Dual Optic-flow Integrated Navigation for Small-scale Flying Robots

Jonghyuk Kim and Galen Brambley
Department of Engineering, Australian National University
Canberra, ACT 0200, Australia
e-mail: {jonghyuk.kim, galen.brambley}@anu.edu.au

Abstract

This paper addresses the recent development of real-time visual odometry system based on a dual optical-flow system and its integration to an inertial navigation system aiming for small-scale flying robots. To overcome the unknown depth information in optic-flow, a dual optic-flow system is developed and tested. The flow measurements are fused with a low-cost inertial sensor using an extended Kalman filter. The experimental results in indoor environment will be presented showing improved navigational performances constraining errors in height, velocity and attitude.

1 Introduction

Optic flow is the apparent visual motion seen by an observer when moving relative to a textured surface. This motion can used to infer information about the state of the observer relative to that surface. This principle is used heavily by insects, where optic flow is used to calculate odometry [Si *et al.*, 2003] and regulate ground speed [Barron and Srinivasan, 2006].

The advantages in using optic flow for motion measurement have made it attractive for robotic applications. Recent advances in digital signal processors and charge-coupled device (CCD) cameras have provided an effective means of embedding the devices on the same chip. This technology has been utilised by several manufacturers in developing a chip that is dedicated to measuring displacement through optic flow. The devices have facilitated the implementation of optic flow sensors into robotic aerial vehicles [Jufferey and Floreano, 2006] and in ground vehicles as displacement measuring devices [Brenner and Smeets, 2003], [Pratt and Turk-Browne, 2003] and odometry estimation [Palacin *et al.*, 2006]. They have also been adapted to visual-servoing obstacle avoidance applications [Green *et al.*, 2003].

The optical chips operate by analysing successive frames of the surface over which they are travelling. The

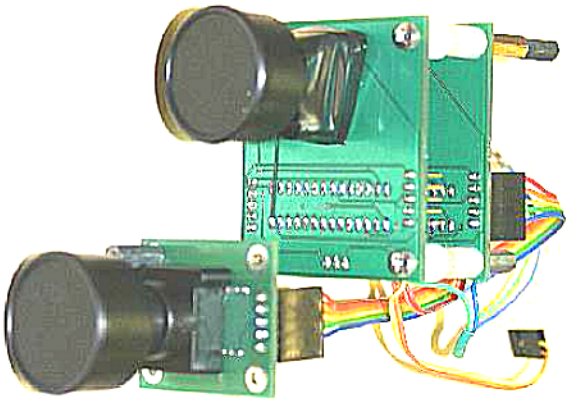

Figure 1: A dual optic-flow system assembled on a printed circuit board with lens and a micro-processor. Depth information can be computed using the difference in optical flows.

frames are acquired at a rate of around 1500 frames-per-second or greater, each of which is analysed by an in-built image-processing algorithm. This algorithm identifies specific features on the image plane and tracks their positions with each successive frame, then assigns two displacement values describing the overall motion of these features. The displacement values are given in terms of pixel counts. These numbers are either stored in specific registers for reading by an external source. If these registers have not been read before an additional set of values have been acquired, and then the values are added to the values already in the register. Assuming that there is no overflow, two integrated values of motion are returned after a motion request. When used in optical mice, they are part of a larger assembly that also includes a lens and a light emitting diode of a specific frequency range. In this setup the mouse is accurate to many hundreds of counts-per-inch, but is especially sensitive to changes in height above the surface [Ng, 2003].

In the application presented in this paper, two opti-

cal mouse chips have been used (as shown in Figure 1) aiming for a self-contained, light-weight navigation system of a small-scale flying robot. The environment has different optical and lighting conditions, and not originally intended for optical mouse chips, because the conditions are vastly different from those considered ideal. First, the terrain beneath the vehicle is not guaranteed to be flat, nor comprise of homogeneous textures. Furthermore, the level of light enveloping the surface is not guaranteed to be of any specific wavelength or intensity. In addition, the attitude and angular rate of the vehicle manifest as errors in the optic flow values. These motion and attitude-induced errors must be removed before any assistance to the vehicle navigation can be made.

While a considerable amount of research has been put into their implementations with robotic vehicles, the problem of fusing two-dimensional (2D) optic flow into the full 6 degrees-of-freedom (DoF) motion estimation problem has not yet been fully addressed. This paper will present the fusion of 2D optic flow data with that of the inertial measurement unit (IMU) into the full 6DoF platform state using an extended Kalman filter (EKF). Moreover, the algorithms use the inertial navigation system equations as opposed to platform specific kinematic models. Thus, the algorithms presented here are general and can be used for any 6DoF platform.

This paper is structured as follows: Section 2 describes the properties of strap-downed optic-flow with a method to compensate the body-induced motion. Section 3 presents the Bayesian data-fusion model and its implementation using an extended Kalman filter. Section 4 will provide experimental results on an indoor robot-arm with conclusions in Section 5.

2 Strap-downed Optic-Flows

The optic flow sensors were designed for use inside a standard desktop mouse. In this environment the lighting is precisely controlled and the reference surface has specific textural properties. When fitted to a moving 6DoF vehicle however, the environmental conditions are no longer ideal. A qualitative assessment of the fundamental differences in the working environments is necessary to ensure the proper integration into a mobile platform. Several key differences in the working environments are:

- In most instances, the optical axis of the camera will not be perpendicular to the terrain beneath the vehicle. This is due to the orientation (or attitude) of the vehicle and the gradient of surrounding terrain.
- The platform will normally have a resultant velocity vector that is not parallel to the surface.
- The intensity and wavelength of the light will not be controllable.
- There will be a rotation rate about some axis that manifests as optic flow.

If the optic flow data are not compensated for the effects of platform motion, large discrepancies between the actual and estimated platform states will arise. It is therefore necessary to calculate and eliminate the effects of platform motion on the optical flow.

2.1 Optic-flow Measurement

The optic-flows measured in a sensor are accumulated pixel counts ($n_x,\ n_y$) over sampling time Δt. These need to be converted to angular increments in radians ($\theta_x,\ \theta_y$) using camera parameters:

$$\theta_x = \left(\frac{\alpha}{n_p}\right) n_x, \quad \theta_y = \left(\frac{\alpha}{n_p}\right) n_y \tag{1}$$

with α/n_p is a conversion factor using the field-of-view (in radians) and the principle pixel dimension (in pixels) within the camera, respectively.

The total optic-flow in radians is also related to the vehicle motion as a ratio of the linear distance travelled ($v_g \Delta t$) and height-above-ground (h_{ag}). That is, $\theta = (v_g \Delta t)/h_{ag}$. This relationship will be used in the following discussions to compute the height-above-ground from the dual optic-flow measurements.

2.2 Vehicle Motion Compensation

Vehicle rotation rates and optic flows are highly coupled since the camera is rigidly mounted (or strap-downed) onto the vehicle body. Any rotation about the x or y axes will manifest as optic flow. This is true even if the vehicle is not translating relative to the navigation frame. As the coordinate systems of the flow sensors are aligned with the body frame, a rotation about the x axis will appear as a change in the optic flow of the y axis, and vice versa.

The rotational motion can be described by the so-called rotation vector $\boldsymbol{\phi} = [\phi_x\ \phi_y\ \phi_z]^T$ and its differential equation [Bortz, 1971],

$$\begin{aligned} \dot{\boldsymbol{\phi}} &= \boldsymbol{\omega}^b_{nb} + \frac{1}{2}\boldsymbol{\phi} \times \boldsymbol{\omega}^b_{nb} \\ &\quad + \frac{1}{\phi_0^2}\left[1 - \frac{\phi_0 \sin\phi_0}{2(1-\cos\phi_0)}\right] \boldsymbol{\phi} \times (\boldsymbol{\phi} \times \boldsymbol{\omega}^b_{nb}), \end{aligned} \tag{2}$$

where $\boldsymbol{\omega}^b_{nb}$ is the angular rate of the body frame with respect to the navigation frame (measured from Gyroscopes), expressed in the body axes, and ϕ_0 represents the magnitude of the rotation vector.

The optic-flow errors resulting from the vehicle rotation can thus be computed using Equations 1 and 2 by

$$\delta n_x = \left(\frac{n_p}{\alpha}\right) \dot{\phi}_y \Delta t \quad \delta n_y = \left(\frac{n_p}{\alpha}\right) \dot{\phi}_x \Delta t, \tag{3}$$

where n_p/α is used again as a conversion factor between radian and pixel.

The error terms are subtracted from the raw optic flow measurements. Note that the rotation motion along the z-axis of the body frame would not affect this correction. This is because that the optic flow around the centre of the image will be averaged out resulting in a zero-flow.

2.3 Ground-Speed and Height

From a single optic-flow measurement, the ground speed and height-above-ground can not be computed separately, giving only the ratio of them. This can be overcome by placing a second source of optic flow with the same orientation, but displaced by a distance L, along the z-axis of the body frame. A relationship analogous to the single sensor case exists for the dual sensor case:

$$h_{ag,1} = \frac{v_g \Delta t}{\theta_1}, \quad h_{ag,2} = \frac{v_g \Delta t}{\theta_2}. \tag{4}$$

Applying some algebraic manipulations and using relationship of $h_{ag,2} = h_{ag,1} + L$, yielding

$$h_{ag,1} \quad = \quad L\left(\frac{\theta_2}{\theta_1 - \theta_2}\right), \tag{5}$$

and subsequently the ground speed being

$$v_g \quad = \quad L\left(\frac{\theta_2}{\theta_1 - \theta_2}\right)\frac{\theta_1}{\Delta t}. \tag{6}$$

3 Optic-Flow Integrated Navigation

In probabilistic navigation, we are interested in the probability density function (pdf) of the vehicle state $\mathbf{x}_k$ at time k given observations $\mathbf{z}_k$, that is *a posterior* pdf:

$$p\left(\mathbf{x}_k \mid \mathbf{z}_k\right) \tag{7}$$

This density can be effectively maintained in prediction and update steps in Bayesian framework. The pdf of the predicted state of the system can be computed by, so called, Chapman-Kolmogorov equation:

$$p\left(\mathbf{x}_k \mid \mathbf{z}_{k-1}\right) = \int p\left(\mathbf{x}_k \mid \mathbf{x}_{k-1}\right) p\left(\mathbf{x}_{k-1} \mid \mathbf{z}_{k-1}\right) d\mathbf{x}_{k-1}. \tag{8}$$

Once observations are available, the predicted pdf is multiplied by the observational likelihood, and then scaled to give *a posterior* density:

$$p\left(\mathbf{x}_k \mid \mathbf{z}_k\right) = c \cdot p\left(\mathbf{z}_k \mid \mathbf{x}_k\right) p\left(\mathbf{x}_k \mid \mathbf{z}_{k-1}\right), \tag{9}$$

with c being a normalisation constant.

Direct implementation of this method is not feasible in most applications. With an assumption of Gaussian densities in *a prior* and *a posterior* pdfs, extended Kalman filter (EKF) can be used effectively. Figure 2 illustrates the structure of the integrated system using EKF where the optic-flow measurements are first compared with those predicted from INS and terrain map and then feed into the filter. The terrain map is required to estimate positional information and a flat-surface model is used throughout this work.

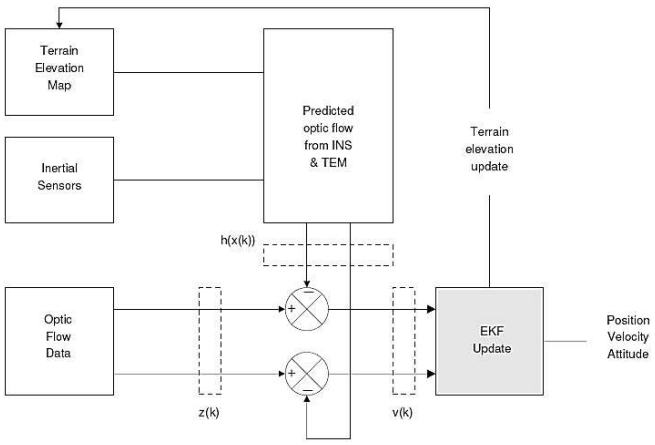

Figure 2: Structure of dual sensor implementation.

3.1 Motion model

The motion model is effectively a nonlinear inertial navigation model in this case, with a state vector of position, velocity, and attitude $\mathbf{x}_k = [\mathbf{p} \;\; \mathbf{v} \;\; \boldsymbol{\psi}]^T$:

$$p\left(\mathbf{x}_{k+1} \mid \mathbf{x}_k\right) \quad \Leftrightarrow \quad \mathbf{x}_{k+1} = \mathbf{f}(\mathbf{x}_k) + \mathbf{w}_k, \tag{10}$$

with nonlinear state-transition function $\mathbf{f}(\cdot)$ (see details in [Kim and Sukkarieh, 2004]), with $\mathbf{w}_k$ being the process noise. The propagated uncertainty is approximated using Jacobian matrix and the strength of the process noise.

3.2 Observation model

The observation model relates the dual optic-flow observations $\mathbf{z} = [n_{x1} \; n_{y1} \; n_{x2} \; n_{y2}]^T$ to the vehicle state:

$$p\left(\mathbf{z}_k \mid \mathbf{x}_k\right) \quad \Leftrightarrow \quad \mathbf{z}_k = \mathbf{h}(\mathbf{x}_k) + \mathbf{v}_k, \tag{11}$$

with $\mathbf{v}_k$ being the observation noise. The nonlinear observation model can be obtained by combining Equations 1 and 4, yielding

$$n_{x1} \quad = \quad \frac{n_p \Delta t}{\alpha}\left(\frac{v_x^b}{h_{ag}} - \dot{\phi}_y\right) + v_{k1} \tag{12}$$

$$n_{y1} \quad = \quad \frac{n_p \Delta t}{\alpha}\left(\frac{v_y^b}{h_{ag}} - \dot{\phi}_x\right) + v_{k2} \tag{13}$$

$$n_{x2} \quad = \quad \frac{n_p \Delta t}{\alpha}\left(\frac{v_x^b}{h_{ag} + L} - \dot{\phi}_y\right) + v_{k3} \tag{14}$$

$$n_{y2} \quad = \quad \frac{n_p \Delta t}{\alpha}\left(\frac{v_y^b}{h_{ag} + L} - \dot{\phi}_x\right) + v_{k4}, \tag{15}$$

Figure 3: Agilent optical-mouse chip (left) and MicroStrain 3DMG inertial measurement unit (right) used for experiment.

which includes the rotation-rate corrections.

The filter updates the density using a predicted density and observation model. The detailed equations are not presented here for brevity and can be found in literatures such as [Maybeck, 1982].

4 Experiments

4.1 Sensor Systems

The Agilent adns-2051 optical mouse chip was chosen for the experiment as shown in Figure 3. It is a non-mechanical optical tracking sensor that is commonly found in computer mice. It measures changes in position by way of determining the direction and magnitude of motion from sequential surface images. The images are nominally acquired at a rate of 1500 frames-per-second which are then analysed by an in-built image-processing algorithm. Specific surface features on the image plane are identified and have their positions tracked with each frame. The collective motion of surface features are assigned two displacement values describing their overall motion across the image plane. The displacement values are then given in terms of pixel counts. The inertial measurement unit used was 3DM-GX1 manufactured by Micro-strain as shown in Figure 3, which low-cost and contains tri-axial gyroscopes, accelerometers and magnetometers.

In preparation for experiment, several printed circuit boards were designed and manufactured to encompass the sensors, micro-controller and the necessary ancillaries for operation. An assembly was produced from the completed boards and then plotted with lens holders and lenses. The completed optical assemblies are illustrated previously in Figures 1.

4.2 Indoor Results

The optic flow assembly and IMU were mounted to an arm containing two pivoting joints, and rigidly mounted to a workbench. The joints of each segment were vertical, and contained well lubricated bushes with low amounts of free play. The motion of the arm was constrained to the $x - y$ plane of the navigation frame, which was coincident with the IMU body frame at the commencement of the experiment. A large and highly textured surface was placed on a level surface beneath the optical assembly at a constant, fixed distance. A $500W$ lamp was placed at a distance of approximately $1.5m$ above and slightly adjacent to the mounting point of the arm, to ensure an adequate intensity of light and negate any adverse influences of the indoor fluorescent lighting in the vicinity of the experiment. During the experimental the arm was put through oscillatory planar motion, such that the highly textured surface was in view of both optic flow sensors.

The predicted velocity and attitude using the raw inertial data is presented in Figures 7 and 8, respectively (the position plot is not shown here since it is similar to velocity plot). They show the behaviour considered typical of low-quality inertial sensors, in that their time to exponential divergence is quite low even with the initial calibration at the beginning.

The optic-flow filtered position, velocity and attitude estimates are illustrated in Figures 9 to 11 respectively. The improvement in the estimates over the raw plots is immediately apparent. Clearly, both the z position and velocity display the desired non-divergent behaviour. The last subplot in Figure 9 is the height-above-ground directly calculated from the raw measurements and shows high-noise level in measurements. The divergence of the x and y positions is due to the flatness of the underlying surface, preventing the position from being observable (this problem is typical in most terrain aided navigation systems where a aircraft needs to fly over undulating terrains to minimise the positional error).

Figures 12 to 13 show the filter's error in estimates for position and attitude, respectively. It is clear that the attitude errors are constrained effectively from optic flow measurements. The divergent behaviour of the x and y covariance again confirms the lack of observability in position. Finally, the four optic-flow innovations with uncertainty are shown in Figure 14 showing that the filter is tuned well.

4.3 Towards Flight Experiment

A model helicopter as shown in Figure 4 is currently being constructed for the verification of the system in flying environment. The performance of the optic system will be greatly affected by environmental factors such as light level, wavelength and texture, as well as flight factors such as speed, height and optic-sampling rate. As an initial work, the flight dependent factors are analysed. Due to the limitations in the sensor resolution and physical installment, the optic sensor can be either failed to recognise the flow or saturated. For example, if

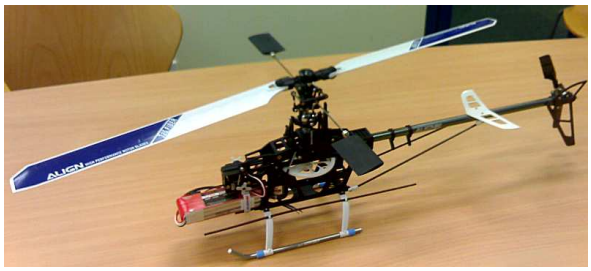

Figure 4: A model helicopter platform built for flying experiments.

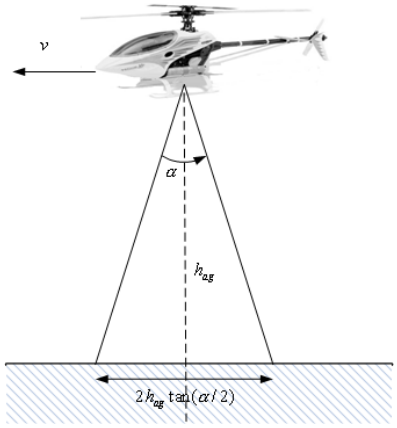

Figure 5: Sensing geometry for the relationship between the flow-rate and vehicle speed.

the difference from both sensors is within sub-pixel, then the depth will be singular and can not be resolved as in Equation 5.

Given the sensing geometry in Figure 5 and assuming translational motion without losing generality, the total maximum displacement within the field-of-view corresponds to the total number of pixels (n_p) in the optic sensor. From this relationship the linear velocity v can be converted to the rate of pixel counts ($\dot{n}$) by

$$\dot{n} = \frac{n_p}{2h_{ag}\tan(\alpha/2)}v \tag{16}$$

with α being the field-of-view.

Therefore the accumulated flows between the sampling time will be

$$n = \dot{n}\Delta t = \frac{n_p}{2h_{ag}f\tan(\alpha/2)} \tag{17}$$

with f being the sampling frequency in Hz (note that this value is different to the internal image-sampling frequency which is fixed to 1500.) For the dual-optic case, the difference in pixel counts between two optic sensors becomes

$$\begin{aligned}\Delta n &= \frac{n_p}{2f\tan(\alpha/2)}\left[\frac{1}{h_{ag,1}} - \frac{1}{h_{ag,2}}\right] \\ &\cong \frac{n_p}{2f\tan(\alpha/2)}\left[\frac{L}{h_{ag,1}^2}\right].\end{aligned} \tag{18}$$

We are interested in the flight condition which can deliver a meaningful pixel counts: that is more than one count. From Equation 18, it can be seen that the output is a function of speed, sampling frequency and height. The sampling time, that is the accessing time to the optic chips, can be easily controlled by the micro-controller, and thus its effects are evaluated with respect to varying heights and using a nominal flight condition with speed (v) being $5m/s$, sensor separation (L) 0.1m, field-of-view 5° and total pixels of 16 pixels.

Figure 6 shows the expected pixel counts from different sampling rates over the height range of 10m. It can be easily seen that $10Hz$-sampling scheme delivers zero pixel readings above the height of 3m (blue-solid line in figure), thus limiting its usage in this region. To be useful for the full range, the sampling rate should be slower than 1Hz (red dash-dot line in figure) or preferably 0.1Hz to provide reliable depth resolutions.

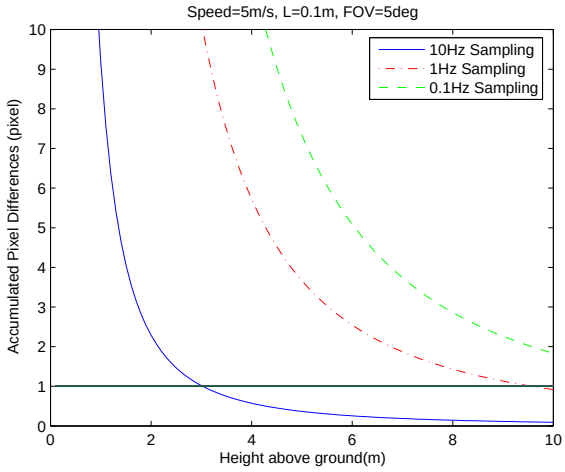

Figure 6: Differences in pixel counts from two optic sensors with varying sampling frequencies and heights. If the count is below one the depth information can not be resolved.

It should be noted that the lack of reliable light sources in outdoor environment can further limit the operating region, particularly in high-altitude regions. Probably it would be a good practical solution to use the optic-system in concert with the conventional satellite-based navigation system such as GPS, which operates properly in most high-altitude regions, whilst the optic-system

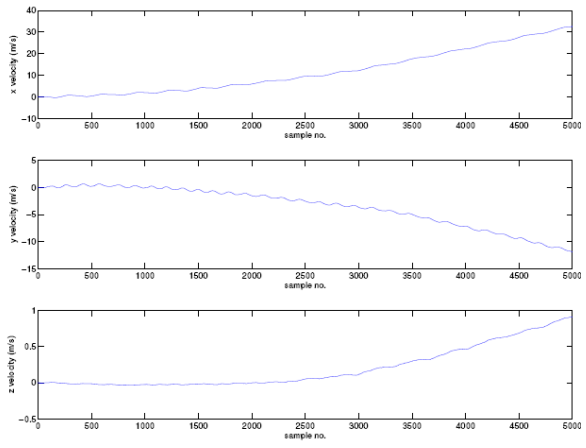

Figure 7: Raw velocity estimate using pure integration of accelerometers with raw attitude.

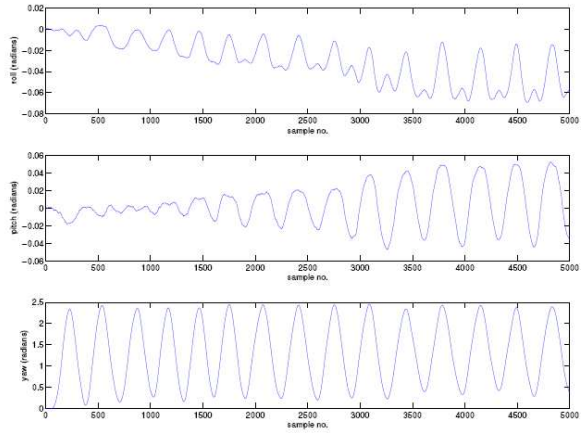

Figure 8: Raw Euler attitude estimate using pure integration of gyro.

delivering reliable aiding signal to the onboard INS close to ground.

5 Conclusions

This paper presented a proof-of-concept study to show the validity of using optical-mouse chips for aided inertial navigation, aiming for flying applications. To provide the unknown depth information in optic-flows, a dual optic-flow sensor was configured and analysed. The flow measurements were then fused with a low-cost inertial sensor output using extended Kalman filter. The indoor experiment showed improved navigation performances constraining errors in altitude, velocity and attitude. Implementation of this system on an actual flying robot platform is currently being undertaken.

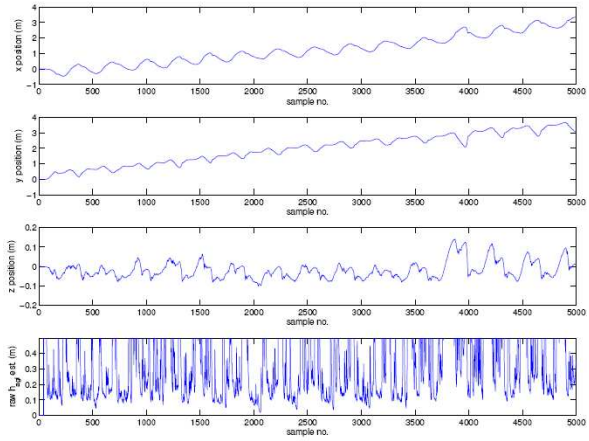

Figure 9: Filtered position estimates using dual optic ow sensors.

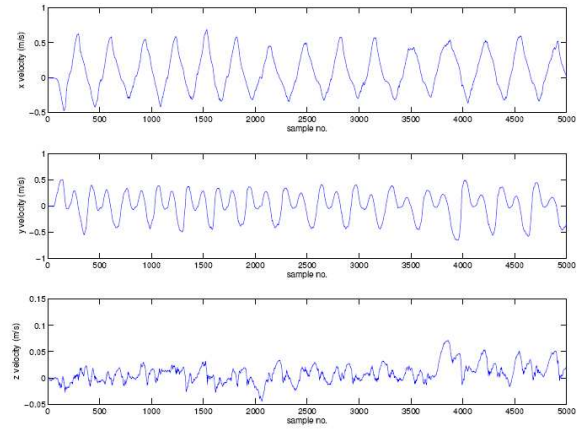

Figure 10: Filtered velocity estimates using dual optic ow sensors.

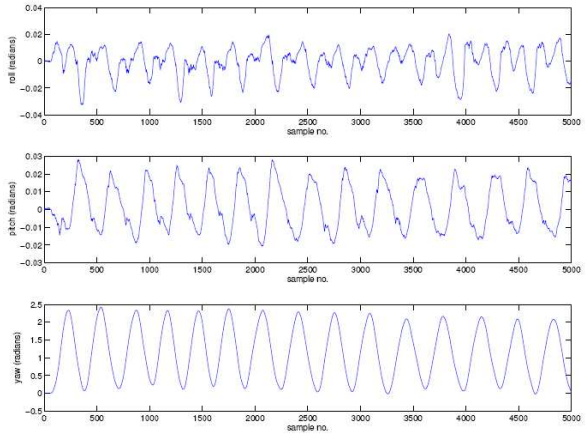

Figure 11: Filtered Euler-angle estimates using dual optic ow sensors.

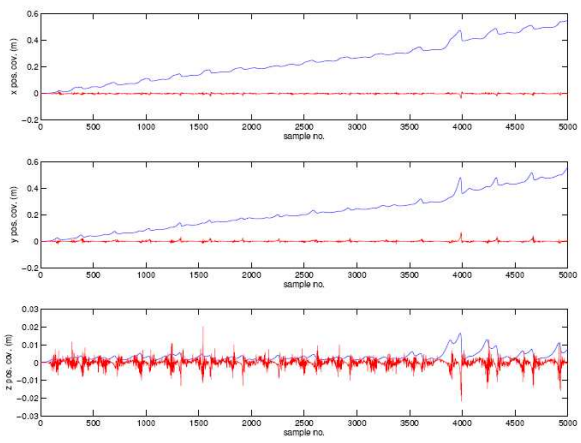

Figure 12: The filter's error in position with $1-\sigma$ uncertainty.

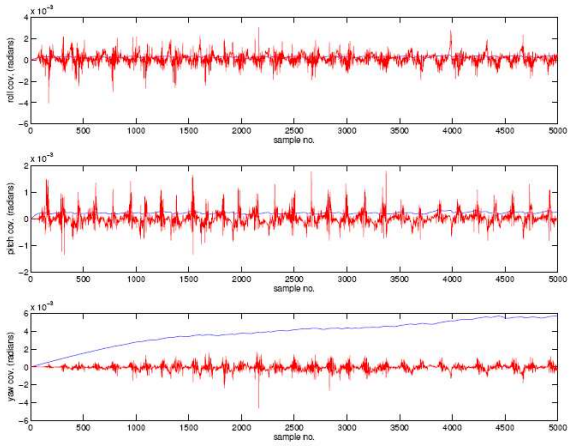

Figure 13: The filter's error in Euler angle with $1-\sigma$ uncertainty.

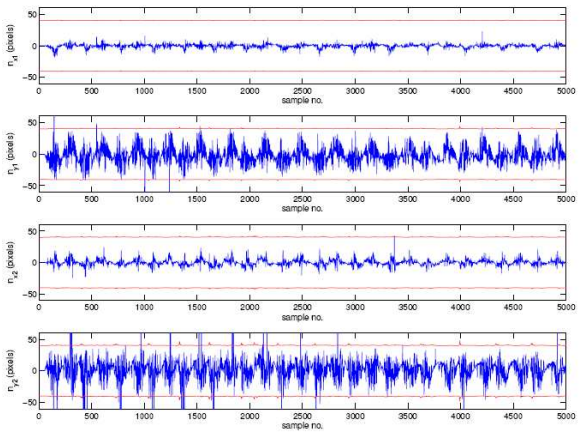

Figure 14: The optic flow innovations within filter with $1-\sigma$ uncertainty.

Acknowledgment

The authors would like to thank anonymous reviewers for their insightful comments on the performance in real flying conditions. This work was also supported by Faculty Research Grant Scheme (FRGS) in Faculty of Engineering and Information Science, Australian National University.

References

[Barron and Srinivasan, 2006] A. Barron and M.V. Srinivasan. Visual regulation of ground speed and headwind compensation in freely fying honey bees. 209, 2006.

[Bortz, 1971] J. Bortz. A New Mathematical Formulation for Strapdown Inertial Navigation. *IEEE Transactions on Aerospace and Electronic Systems*, AES-7(1):61–66, 1971.

[Brenner and Smeets, 2003] E. Brenner and J.B.J. Smeets. Fast corrections of movements with a computer mouse. *Spatial Vision*, 16:365–376, 2003.

[Green *et al.*, 2003] W.E. Green, P.Y. Oh, K. Sevcik, and G. Barrows. Autonomous landing for indoor flying robots using optic flow. In *ASME International Mechanical Engineering Congress*, 2003.

[Jufferey and Floreano, 2006] J.C. Jufferey and D.F Floreano. Fly-inspired visual steering of an ultralight indoor aircraft. *IEEE Transactions on Robotics*, 22(1):137–146, 2006.

[Kim and Sukkarieh, 2004] J. Kim and S. Sukkarieh. Autonomous Airborne Navigation in Unknown Terrain Environments. *IEEE Transactions on Aerospace and Electronic Systems*, 40(3):1031–1045, July 2004.

[Maybeck, 1982] P. Maybeck. *Stochastic Models, Estimations and Control*, volume 1,2. Academic Press, 1982.

[Ng, 2003] T.W. Ng. The optical mouse as a two-dimensional displacement sensor. *Sensors and Actuators*, 107:21–25, 2003.

[Palacin *et al.*, 2006] J. Palacin, I. Valga non, and R. Pernion. The optical mouse for indoor mobile robot odometry measurement. *Sensors and Actuators*, 126:141–147, 2006.

[Pratt and Turk-Browne, 2003] J. Pratt and N.B. Turk-Browne. The attentional repulsion effect in perception and action. *Experimental Brain Research*, pages 152–376, 2003.

[Si *et al.*, 2003] A. Si, M.V. Srinivasan, and S.W. Zhang. Honeybee navigation: Properties of the visually driven odometer. 206, 2003.